COMMUNICATION

Check for updates

Self-assembly of copper nanoclusters: isomeric ligand effect on morphological evolution†

Sarita Kolay,[a] Subarna Maity, [iD][a] Dipankar Bain, [iD][a] Sikta Chakraborty[a] and Amitava Patra [iD] *[ab]

Tailoring the hierarchical self-assembly of metal nanoclusters (NCs) is an emergent area of research owing to their precise structure and flexible surface environment. Herein, the morphological evolution from rods to platelets to ribbon-like structures through self-assembly of Cu_7 NCs is dictated by the positional isomerism of the surface capping ligand, dimethylbenzenethiol (DMBT). Besides cuprophilic interaction, the interplay between $\pi-\pi$ stacking and agostic interaction (Cu···H–C) directs the inter-NC organization into different ordered architectures. The excited-state relaxation dynamics of the red phosphorescent assembled structures has been correlated with their compactness and the degree of bonding interactions present.

Self-assembly is a recognized process associated with the spontaneous organization of components into ordered structures or aggregates.[1–5] Notable progress in synthetic chemistry has allowed rapid growth in the self-assembly of organic molecules, metal nanoparticles, and ultrasmall nanomaterials (<2 nm).[6–10] Metal NCs are promising candidates as the building blocks of assembled architectures to control the morphology by manipulating the driving forces which eventually control their properties.[11–13] Although isolated metal NCs often exhibit lower quantum yield (QY), the self-assembly of NCs leads to bright and tunable luminescence properties.[14] Several strategies have been used to design various assembled structures by tailoring the capping ligands and regulating temperature, pH, light, solvent, etc.[15–19] Zhang et al. have designed self-assembled ribbons with tunable emission by changing the electron-donating groups of the capping ligand.[20] It is reported that the solubility of ligands in different solvents controls the

morphology of self-assembled structures. The nature of solvent influences the changes of the inter-cluster distance of assembly, which dictates the assembly structure.[18,21] Molecular self-assembly involves non-covalent or weak covalent interactions such as van der Waals, electrostatic and hydrophobic interactions, and hydrogen and coordination bonds.[22–24] The C–H···π interaction,[5] aurophilic,[25] argentophilic,[26] and cuprophilic[14] interactions are responsible for assembling metal NCs. Thus, the mechanism of formation of the self-assembled structures of metal NCs is not trivial, and a deep understanding is essential to control their properties. The formation of assembled structures is directed by the electronic charge and the functional groups of the ligands.[20] The bulkiness and position of the substituents on the ligands may be decisive parameters for the self-assembly of metal NCs.

Photoluminescence (PL) of atomically precise metal NCs is the prime property required for optoelectronic and biomedical applications, and is governed by the metal-core and ligand shell.[27–31] The assembly-induced emission enables them to be applied as phosphors to fabricate LEDs generated from strong metallophilic interaction depending on their packing. The relaxation dynamics of the excited state of the NCs is controlled by the ligand–ligand, ligand–metal, and metal–metal interactions.[32–34] The restriction of the rotation and vibration of the ligands also influences the rate of non-radiative relaxation of the excited state.[35–38]

Herein, we design inter-NC assembly into ordered structures by the precise control of the surface protecting ligand. Although the compositions of the Cu NCs are identical, only the position of a $-CH_3$ group in the DMBT ligand regulates the morphology of the assembled structures. The interplay of cuprophilic, $\pi-\pi$ stacking and agostic interactions leads to the organization of Cu_7 NCs into rods, platelets, and ribbon-like assemblies. A higher degree of bonding interaction provides a longer excited-state lifetime because of the rigidification of the surface ligands.

The one-pot synthesis procedure involves reductive decomposition of the Cu-thiolate complex to form self-assembled Cu NCs (for details, see the ESI†). In a MeOH/DCM mixed solvent,

[a]School of Materials Sciences, Indian Association for the Cultivation of Science, Jadavpur, Kolkata-700032, India. E-mail: msap@iacs.res.in; Fax: +91-33-2473-2805; Tel: +91-33-2473-4971

[b]Institute of Nano Science and Technology, Knowledge City, Sector 81, Mohali 140306, India

† Electronic supplementary information (ESI) available: Details of synthesis procedures, TEM images, AFM images, TGA, FTIR, XPS, ^{1}H NMR spectra and additional figures. See DOI: 10.1039/d1na00446h
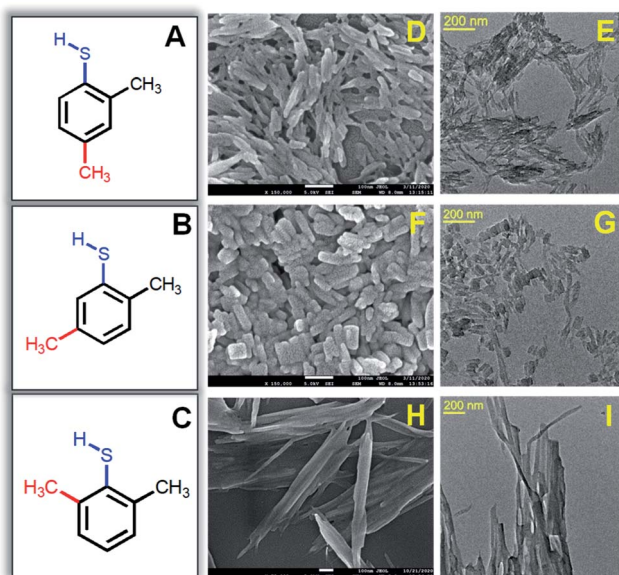
Fig. 1 Structures of (A) 2,4- (B) 2,5- and (C) 2,6-DMBT ligands. FE-SEM and TEM images of rods (D and E), platelets (F and G) and ribbon-like (H and I) self-assemblies, respectively. The scale bar of the SEM images is 100 nm.

$CuNO_3 \cdot 3H_2O$ is dissolved and reacted with three isomers of DMBT in each synthesis process. The color of the reaction medium changes from sky blue to yellow ochre due to the complexation of Cu^{2+} with 2,4-DMBT. However, the complex formation with 2,5-DMBT and 2,6-DMBT leads to light yellow and curdy white suspensions. A secondary phosphine ligand (PPh$_4$Br) is added, followed by the reduction with NaBH$_4$. For the 2,4-isomer, we obtained a bright yellow-colored solution under ice-cold conditions after 5 hours. The same method provided a light yellow suspension for 2,5-DMBT capped self-assembled NCs, while the 2,6-DMBT capped NC assembly gave a muddy white suspension (Fig. S1†). Fig. 1A–C show the structures of isomeric 2,4-, 2,5- and 2,6-DMBT ligands. The extent of steric hindrance due to the two –CH$_3$ groups adjacent to –SH in the 2,6-isomer is more significant than that of 2,4- and 2,5-isomers. The isomeric ligands may affect the morphology and optical properties of self-assembled structures. The formation of rod-like structures in the presence of 2,4-DMBT is seen clearly in Fig. 1D with an average length 66 ± 2.1 nm, whereas the width is 15 ± 1.1 nm (Fig. 1E).

The morphology of the assembled structures changes with changing the methyl position from fourth to fifth in 2,5-DMBT (Fig. 1F). The length is found to be 46 ± 2.5 nm which is lower than that of the assembled rods, while the width increases from 15 nm to 25 ± 1.8 nm (Fig. 1G). Thus, the change in the aspect ratio of the self-assemblies arises from the positional isomerism of the DMBT ligand. A ribbon-like morphology is found in the presence of the 2,6-DMBT ligand where the length is more than 1 μm and the width is 31 ± 2.5 nm (Fig. 1H and I). The hierarchical self-assembled structures are composed of ~1 nm Cu NCs which is evident from the high-resolution TEM images in Fig. S2.† An even arrangement of the ribbon-like assemblies with lengths of

several micrometers is observed (Fig. S2C†). Energy-dispersive X-ray (EDX) element mapping shows an even distribution of Cu and S across the self-assembled structures (Fig. S3†). The thickness of the assembled structures is measured using atomic force microscopy (AFM), and the heights are 34 nm, 16.5 nm, and 25 nm for rods, platelets, and ribbon-like assemblies, respectively (Fig. S4†). Compositional and structural analyses were done to get insights into the mechanism.

Thermogravimetric analysis (TGA) reveals a mass loss of 65% in each case due to the decomposition of organic ligands as gaseous products, where the two –CH$_3$ groups are the most labile to dissociate first (Fig. S5†). The dissociation of the two –CH$_3$ groups happens at <260 °C, which leads to a 14% mass loss. In the next stage, the phenyl rings are likely to decompose within 260–320 °C resulting in 35.5% loss of mass. In the last step, 15% mass loss is observed as the S atoms of the ligand dissociate, which are covalently coordinated with Cu. The firmly bound S atoms dissociate at >320 °C. It is noted that the matrix-assisted laser desorption ionization (MALDI) mass spectrometric study confirmed the formation of Cu_7L_6 for all three cases (Fig. 2A). The mass loss corresponds to a Cu/DMBT molar ratio of 1.162/1. In MALDI mass spectra, a small peak at $m/z = 1267$ is identified as a molecular ion peak along with a few peaks at m/z 1090, 1076, and 1012 due to fragmentation. Based on MALDI-MS and TGA analyses, the structure of the NCs is assigned as $Cu_7(DMBT)_6$. The peak at $m/z = 1090$ is ascribed to $Cu_6(DMBT)_5 + Na^+$, which arises from the dissociation of Cu-DMBT from $Cu_7(DMBT)_6$. The peak at $m/z = 1076$ Da is assigned to $[Cu_7(DMBT)_4 + Br^- + 2H^+]$, which arises from the dissociation of two DMBT ligands. Again, the most intense peak at $m/z = 1012$ Da is ascribed to $[Cu_6(DMBT)_4 + Br^- + 2H^+]$, which arises due to the dissociation of $Cu(DMBT)_2$ from $Cu_7(DMBT)_6$. As the composition of the building blocks of all three assembled structures is the same (Cu_7L_6), the compositional effect on the morphology is eliminated. Therefore, the formation of self-assemblies is a surface phenomenon that arises due to inter-NC bonding interactions. The appearance of a covalent Cu–S bond is confirmed by FTIR spectroscopy. The S–H vibration in free DMBT arises at 2525 cm^{-1}, which then disappears after self-assembly of Cu NCs. The absence of S–H stretching frequency confirms the Cu–S covalent bond formation between Cu and DMBT (Fig. S6†).

To assemble into the ordered structures, each individual Cu NC must experience inter-NC non-covalent interactions. The DMBT ligands do not have any electron-donating or withdrawing group with active conjugation. So, the key driving force may be metallophilic interaction as well as π–π stacking which is governed by the nature of the ligand. XPS analysis is used to understand the Cu(I)–Cu(I) cuprophilic interaction. The peaks at 932.7 and 952.6 eV arise due to Cu 2p$_{3/2}$ and 2p$_{1/2}$, respectively, in self-assembled rods and platelets (Fig. S7†). The Cu peaks for self-assembled ribbons show a negligible shift to a lower energy value (932.56 and 952.4 eV). Cu(II) is not present in the core as there is no satellite peak at 942 eV.[39]

There is no significant change in Cu 2p binding energy in rods, platelets, and ribbon self-assemblies, indicating the presence of the same cuprophilic interaction for all cases. The peaks for S 2p$_{3/2}$, and 2p$_{1/2}$ appear at 162.4 and 163.6 eV,
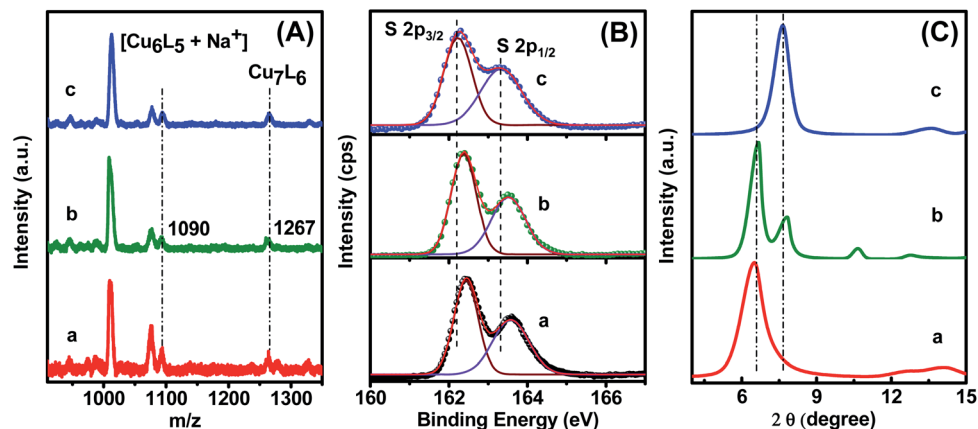
Fig. 2 (A) Positive mode MALDI-TOF mass spectra, (B) XPS spectra for S 2p and (C) powder X-ray diffraction patterns of self–assembled (a) rods, (b) platelets, and (c) ribbons.

respectively, for both rods and platelets (Fig. 2B). A dramatic decrease in S 2p binding energy is evident in ribbons as the peaks show up at 162.2 and 163.3 eV. The lower binding energy of S 2p indicates more inter NC surface interaction for ribbons than for the rods and platelets. The long-range non-covalent inter-NC interactions must govern the ligand-dependent self-assembly formation. Here, the close alignment of the Cu NCs may be due to the cuprophilic interaction. The drastic difference in morphology of the self-assemblies is not attributed to the metallophilic interaction as there is no significant change in the binding energies of Cu 2p for rods and platelets.

Powder X-ray diffraction (XRD) measurements were carried out to understand the packing of NCs into the assembled structures. The Cu NCs exhibit a highly ordered arrangement within the self-assembled structures, giving intense peaks in powder XRD (Fig. 2C). The XRD pattern of rod-like assemblies shows a single peak at 6.53°, whereas three distinct diffraction peaks at 6.63°, 7.83°, and 10.5° are obtained for the platelets. On the other hand, ribbon-like assemblies exhibit one distinct peak at 7.66°. For rods and ribbon-like assembled structures, the sole peak indicates only one dominant distance between the individual NCs. The appearance of three peaks in platelets indicates three different distances among the adjacent NCs.[24] Of the two peak positions for platelets, one has a close resemblance to that of rods and another to that of ribbon-like assemblies. It reveals that the platelet-like assemblies have grown along longitudinal as well as the transverse direction.

Apart from dominating cuprophilic interaction, aromatic thiol ligands experience significant π–π stacking interaction, which depends on the bulkiness of each isomer. We have observed broad XRD peaks at $2\theta \sim 25$–$27°$ arising from the π–π stacking of the self-assembled nanostructures (Fig. S8†).[40,41] The cuprophilic interaction is further reinforced by π–π stacking between ligands. Previously, isomeric benzenethiols were used to synthesize various magic-sized AuNCs by controlling the interfacial Au–S bonds.[42] Depending on the one –CH$_3$ group position, the steric hindrance on the ligand is localized in one position for 2,4- and 2,6-DMBT ligands. The localized steric hindrance exerted by the methyl groups dictates the growth of

self-assemblies predominantly in a single direction, leading to the formation of rods and ribbon-like assemblies.

On the other hand, two –CH$_3$ and –SH binding sites are distributed over the aromatic ring in the 2,5-DMBT ligand. The steric hindrance-controlled π–π stacking partially explains the formation of different self-assembled structures. The difference in morphology between self-assembled rods and ribbons must be attributed to another non-covalent interaction. However, the nature of π–π stacking interaction in 2,4- and 2,6-DMBT is similar. Apart from cuprophilic and π–π stacking interaction, the Cu···H–C, namely agostic interaction, is the crucial factor in dictating the morphology. The pattern of ribbon-like assemblies indicates their growth along the longitudinal direction, which is controlled by the maximum extent of agostic interaction (Cu···H–C) on the surface. There are two kinds of M···H–C interactions, i.e., anagostic and agostic, depending on M···H distances and M–H–C angles, differentiated from ^{1}H NMR spectroscopy.[43] The Au···H–C anagostic interaction in o-substituted benzenethiol capped Au$_{38}$ NCs imparts an effect on their stability.[44] The chemical shift of agostic hydrogen atoms generally appears as an upfield shift compared to the uncoordinated hydrogen, whereas anagostic hydrogen shows a downfield shift. ^{1}H NMR spectroscopic study is performed to understand the agostic or anagostic interaction for assembly formation. The ^{1}H NMR spectra of DMBT exhibit broad peaks in the range of 7.19 to 6.89 ppm associated with aromatic protons.

In the 2,4-DMBT ligand, two methyl (–CH$_3$) groups appear at 2.32 and 2.29 ppm. Upon self-assembled rod formation, the methyl protons appear at 2.36 and 2.28 ppm (Fig. S9†). The two –CH$_3$ groups of 2,5-DMBT show up as two singlets at 2.47 and 2.44 ppm, whereas the –CH$_3$ protons in platelets experience an upfield shift (2.37–2.25 ppm) compared to the uncoordinated ones, indicating the presence of agostic interaction (Fig. S10†). For 2,6-DMBT, the chemical environment of the two –CH$_3$ groups is the same, leading to the appearance of a single peak at 2.38 ppm. The ^{1}H NMR spectrum shows two different singlet peaks at 2.17 and 2.36 ppm in ribbon-like assembly formation (Fig. S11†). In self-assembled structures, the oxidation state of Cu is between 0 and 1. It creates a δ+ charge, whereas the H atom of

the –CH$_3$ group experiences a $\delta-$ charge, leading to an increase in the electron density. That causes an upfield shift of the hydrogen after coordinating with the metal. The large upfield shift of protons of one –CH$_3$ indicates the presence of maximum agostic interaction in 2,6-DMBT capped ribbon-like NC assemblies. This result reflects in the TGA analysis (Fig. S5†). Although the total mass loss is the same for all the assemblies, the dissociation behavior is different. For the rod and platelet-like assemblies, a step-wise dissociation is observed below 260 °C, indicating different dissociation energies for the two –CH$_3$ groups. On the other hand, the complete dissociation of the methyl groups requires a higher temperature than 260 °C, which indicates a greater extent of agostic interaction in the ribbon-like assemblies. Additionally, no steplike dissociation curve is observed, which means that the two –CH$_3$ groups have similar dissociation energies in 2,6-DMBT capped self-assembled Cu NCs.

Fig. 3 shows a schematic illustration of self-assembly evolution from the individual Cu$_7$(DMBT)$_6$ into a ribbon-like assembly. In the case of the rod-like assemblies, relatively less agostic interaction occurs because the 2,4-isomer has only one *ortho*-substituted methyl. It favors longitudinal directional growth with a maximum length of 66 nm. One *ortho*-substituted thiol group is present in the 2,5-isomer also, which will not allow the self-assemblies to grow longer in the longitudinal direction. The *para* position of thiol is free and may form strong π–π interaction, causing the assemblies to grow in the transverse direction. A length of >1 μm for ribbons indicates maximum longitudinal growth, whereas the rod-like and plate-like assemblies show a much smaller average length of 66 nm and 46 nm, respectively. This clearly shows that the extent of agostic interaction is larger for the 2,6-isomer capped self-assembly structures as both the *ortho* positions are substituted, supported by the maximum upfield shift in NMR spectrum. The agostic-interaction-assisted self-assembly formation and the morphological evolution significantly affect the PL behaviour of the NCs.

The assembled or aggregated NCs exhibit intense PL in comparison to isolated NCs due to the hindrance of rotational and vibrational motions in compact structures.[37,45,46] The

assembled NCs showed absorption humps around 360 nm while the ribbon-like NC assemblies exhibit an additional hump at 320 nm, which is due to the electronic transition from DMBT to the Cu core (Fig. 4A). The peak around 330 nm signifies the presence of π–π stacking between the adjacent benzene rings.[47] The PL excitation maxima are also in good agreement with the absorption spectra (Fig. S12†). All the assembled structures exhibit red emission in solid as well as solution states (inset of Fig. 4B). The emission maximum for the 2,4-DMBT capped NC assemblies is centered at 650 nm while it is 655 nm for platelets. The rod-like assemblies are found to have a QY of 1.1%, while it is 2.5% for the platelet-like assemblies. The ribbon-like assemblies of Cu NCs capped with 2,6-DMBT show a blue-shifted emission maximum at 640 nm and the highest QY of 7.8% (Fig. 4B). The microsecond scale lifetime and large Stokes shift (>200 nm) suggest that the emission of self-assembled NCs arises from a triplet state involving ligand to metal charge transfer (LMCT) or ligand to metal–metal charge transfer (LMMCT) from the sulfur atoms of the DMBT ligand to the Cu core.[48] Platelet-like assemblies exhibit red-shifted emission from the low-lying triplet state as the π–π stacking interaction is the maximum. On the other hand, agostic interaction dominates over π–π stacking in ribbon-like assemblies. Thus the PL arises from a relatively high-lying triplet state which causes a blue-shifted emission maximum.

The PL decay time of each self-assembly is fitted with a tri-exponential fitting, and the average decay time varies from nanoseconds to a few microseconds (Fig. 4C). The detailed fitting parameters are summarized in Table S1 in the ESI.† The rod-like assemblies exhibit an average decay time of 0.35 μs, while the platelets show an increase in decay time to 0.65 μs. The rise in QY and average decay time for the 2,5-DMBT protected NC assemblies indicates increased radiative relaxation processes. Since the assembly of NCs forms platelets in two directions, the motion of surface ligands is suppressed in comparison with 2,4-DMBT capped rod-like assemblies. This
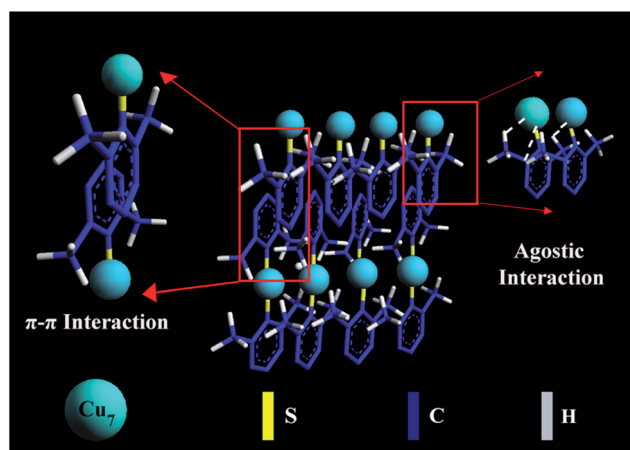

Fig. 3 Schematic illustration of self-assembly evolution from the individual Cu$_7$(DMBT)$_6$ into a ribbon-like assembly. A few ligands in the Cu NCs are omitted for simplicity.
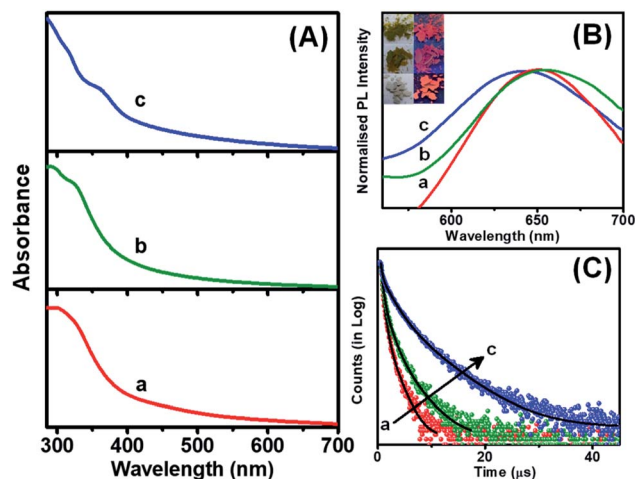

Fig. 4 (A) UV–vis absorption, (B) PL emission spectra, and (C) PL decay curves of the self-assembled rods (a), platelets (b), and ribbons (c). The inset shows the digital photographs of self-assembled Cu NCs in daylight and under UV (365 nm) excitation.

indicates that the loose packing of NCs in rod-like assemblies makes it difficult to suppress the non-radiative relaxation process arising from the vibration and rotation of the ligands. The unidirectional assembly in rods causes a substantial motion of ligands leading to a greater extent of non-radiative processes during excited state relaxation.

On the other hand, the ribbon-like assemblies exhibit nearly one order of magnitude increase of the lifetime to 1.68 μs. Although the π–π stacking interaction is similar to that in the 2,4-DMBT capped rod-like NC assemblies, the manifestation of agostic interaction with o-CH$_3$ groups creates the long-range assembly. Since the maximum QY is obtained for ribbon-like assemblies, it suggests that the higher order of assembly reduces the motion of ligands and rigidifies the structure, enhancing the decay time and blue shift in the emission wavelength. The significant Stokes shift and microsecond decay time suggest that phosphorescence largely depends on the inter-NC interactions. Therefore, the morphology and optical properties of self-assembled NCs can be regulated by rational tuning of the capping ligand. The design of NC-based luminescent self-assembled materials will be advantageous in the development of light-emitting phosphors and catalysis.

Conclusions

In summary, the DMBT-capped Cu$_7$ NCs are organized into customizable superstructures from rods to platelets to ribbons. Although the cuprophilic interaction is indistinguishable, only the difference in the –CH$_3$ position of the isomeric DMBT ligands significantly alters the extent of π–π stacking and agostic interaction. The more of o-CH$_3$ present, the more vital the agostic interaction, which eventually culminates into the most extended ribbon-like assembly of 2,6-DMBT capped Cu$_7$ NCs. The red emission is correlated with the compactness and effective bonding interactions in the assembled structures, leading to the most extended excited-state lifetime of ribbon-like assemblies. The insights into the bonding interactions in the self-assembled metal NCs will pave the way towards designing ordered architectures with potential applicability in optoelectronics, catalysis, and bio-imaging.

Author contributions

SK contributed to the investigation, methodology, data curation, and writing of the original draft. SM helped in conceptualization and review, and editing the draft. DB contributed to editing and visualization. SC helped in data curation. AP contributed to supervision, validation, project administration, and final review.

Conflicts of interest

There are no conflicts to declare.

Acknowledgements

Notes and references

1 G. M. Whitesides and B. Grzybowski, *Science*, 2002, **295**, 2418.

2 K. J. M. Bishop, C. E. Wilmer, S. Soh and B. A. Grzybowski, *Small*, 2009, **5**, 1600–1630.

3 D. Luo, C. Yan and T. Wang, *Small*, 2015, **11**, 5984–6008.

4 M. Grzelczak, J. Vermant, E. M. Furst and L. M. Liz-Marzán, *ACS Nano*, 2010, **4**, 3591–3605.

5 C. Zeng, Y. Chen, K. Kirschbaum, K. J. Lambright and R. Jin, *Science*, 2016, **354**, 1580.

6 Z. Xie, P. Sun, Z. Wang, H. Li, L. Yu, D. Sun, M. Chen, Y. Bi, X. Xin and J. Hao, *Angew. Chem., Int. Ed.*, 2020, **59**, 9922–9927.

7 L. Zang, Y. Che and J. S. Moore, *Acc. Chem. Res.*, 2008, **41**, 1596–1608.

8 H.-Y. Lee, S. H. R. Shin, A. M. Drews, A. M. Chirsan, S. A. Lewis and K. J. M. Bishop, *ACS Nano*, 2014, **8**, 9979–9987.

9 X. Ouyang, M. Wang, L. Guo, C. Cui, T. Liu, Y. Ren, Y. Zhao, Z. Ge, X. Guo, G. Xie, J. Li, C. Fan and L. Wang, *Angew. Chem., Int. Ed.*, 2020, **59**, 11836–11844.

10 D. Zhou, M. Liu, M. Lin, X. Bu, X. Luo, H. Zhang and B. Yang, *ACS Nano*, 2014, **8**, 10569–10581.

11 Z. Wu, Q. Yao, S. Zang and J. Xie, *ACS Mater. Lett.*, 2019, **1**, 237–248.

12 S. Hossain, Y. Imai, Y. Motohashi, Z. Chen, D. Suzuki, T. Suzuki, Y. Kataoka, M. Hirata, T. Ono, W. Kurashige, T. Kawawaki, T. Yamamoto and Y. Negishi, *Mater. Horiz.*, 2020, **7**, 796–803.

13 X. Kang and M. Zhu, *Coord. Chem. Rev.*, 2019, **394**, 1–38.

14 Z. Wu, J. Liu, Y. Gao, H. Liu, T. Li, H. Zou, Z. Wang, K. Zhang, Y. Wang, H. Zhang and B. Yang, *J. Am. Chem. Soc.*, 2015, **137**, 12906–12913.

15 J. Liu, Y. Tian, L. Ai, Z. Wu, D. Yao, Y. Liu, B. Yang and H. Zhang, *Langmuir*, 2020, **36**, 14614–14622.

16 X. Su and J. Liu, *ACS Appl. Mater. Interfaces*, 2017, **9**, 3902–3910.

17 L. Ai, Y. Li, Z. Wu, J. Liu, Y. Gao, Y. Liu, Z. Lu, H. Zhang and B. Yang, *J. Phys. Chem. C*, 2016, **120**, 24427–24436.

18 L. Ai, Z. Liu, D. Zhou, J. Liu, H. Zou, Z. Wu, Y. Liu, H. Zhang and B. Yang, *Nanoscale*, 2017, **9**, 18845–18854.

19 X. Jia, X. Yang, J. Li, D. Li and E. Wang, *Chem. Commun.*, 2014, **50**, 237–239.

20 L. Ai, W. Jiang, Z. Liu, J. Liu, Y. Gao, H. Zou, Z. Wu, Z. Wang, Y. Liu, H. Zhang and B. Yang, *Nanoscale*, 2017, **9**, 12618–12627.

21 Q. Yao, Y. Yu, X. Yuan, Y. Yu, D. Zhao, J. Xie and J. Y. Lee, *Angew. Chem., Int. Ed.*, 2015, **54**, 184–189.

22 Z. Wu, Y. Li, J. Liu, Z. Lu, H. Zhang and B. Yang, *Angew. Chem., Int. Ed.*, 2014, **53**, 12196–12200.

23 Z. Wu, J. Liu, Y. Li, Z. Cheng, T. Li, H. Zhang, Z. Lu and B. Yang, *ACS Nano*, 2015, **9**, 6315–6323.

24 Z. Wu, C. Dong, Y. Li, H. Hao, H. Zhang, Z. Lu and B. Yang, *Angew. Chem., Int. Ed.*, 2013, **52**, 9952–9955.

25 Z. Wu, Y. Du, J. Liu, Q. Yao, T. Chen, Y. Cao, H. Zhang and J. Xie, *Angew. Chem., Int. Ed.*, 2019, **58**, 8139–8144.

26 P. Sun, Z. Wang, Y. Bi, D. Sun, T. Zhao, F. Zhao, W. Wang and X. Xin, *ACS Appl. Nano Mater.*, 2020, **3**, 2038–2046.

27 S. Maity, D. Bain, S. Chakraborty, S. Kolay and A. Patra, *ACS Sustain. Chem. Eng.*, 2020, **8**, 18335–18344.

28 S. Maity, D. Bain and A. Patra, *Nanoscale*, 2019, **11**, 22685–22723.

29 D. Bain, S. Maity and A. Patra, *Phys. Chem. Chem. Phys.*, 2019, **21**, 5863–5881.

30 A. Baghdasaryan and T. Bürgi, *Nanoscale*, 2021, **13**, 6283–6340.

31 X. Kang and M. Zhu, *Chem. Soc. Rev.*, 2019, **48**, 2422–2457.

32 Z. Luo, X. Yuan, Y. Yu, Q. Zhang, D. T. Leong, J. Y. Lee and J. Xie, *J. Am. Chem. Soc.*, 2012, **134**, 16662–16670.

33 D. Bain, S. Maity and A. Patra, *Chem. Commun.*, 2020, **56**, 9292–9295.

34 Z. Wu, H. Liu, T. Li, J. Liu, J. Yin, O. F. Mohammed, O. M. Bakr, Y. Liu, B. Yang and H. Zhang, *J. Am. Chem. Soc.*, 2017, **139**, 4318–4321.

35 J. Liang, Z. Chen, J. Yin, G.-A. Yu and S. H. Liu, *Chem. Commun.*, 2013, **49**, 3567–3569.

36 X. Jia, J. Li and E. Wang, *Small*, 2013, **9**, 3873–3879.

37 S. Maity, D. Bain and A. Patra, *J. Phys. Chem. C*, 2019, **123**, 2506–2515.

38 R. Jin, C. Zeng, M. Zhou and Y. Chen, *Chem. Rev.*, 2016, **116**, 10346–10413.

39 X. Gao, Y. Lu, M. Liu, S. He and W. Chen, *J. Mater. Chem. C*, 2015, **3**, 4050–4056.

40 K. Dey, H. S. Kunjattu, A. M. Chahande and R. Banerjee, *Angew. Chem., Int. Ed.*, 2020, **59**, 1161–1165.

41 A. K. Mohammed, S. Usgaonkar, F. Kanheerampockil, S. Karak, A. Halder, M. Tharkar, M. Addicoat, T. G. Ajithkumar and R. Banerjee, *J. Am. Chem. Soc.*, 2020, **142**, 8252–8261.

42 Y. Chen, C. Zeng, D. R. Kauffman and R. Jin, *Nano Lett.*, 2015, **15**, 3603–3609.

43 M. Brookhart, M. L. H. Green and G. Parkin, *Proc. Natl. Acad. Sci. U. S. A.*, 2007, **104**, 6908.

44 Y. Li, R. Juarez-Mosqueda, Y. Song, Y. Zhang, J. Chai, G. Mpourmpakis and R. Jin, *Nanoscale*, 2020, **12**, 9423–9429.

45 J. Mei, N. L. C. Leung, R. T. K. Kwok, J. W. Y. Lam and B. Z. Tang, *Chem. Rev.*, 2015, **115**, 11718–11940.

46 M. Sugiuchi, J. Maeba, N. Okubo, M. Iwamura, K. Nozaki and K. Konishi, *J. Am. Chem. Soc.*, 2017, **139**, 17731–17734.

47 L. Li and Q. Wang, *ACS Nano*, 2013, **7**, 3053–3060.

48 K. Pyo, V. D. Thanthirige, K. Kwak, P. Pandurangan, G. Ramakrishna and D. Lee, *J. Am. Chem. Soc.*, 2015, **137**, 8244–8250.